RSC Advances

PAPER

View Article Online
View Journal | View Issue

Open Access Article. Published on 22 June 2018. Downloaded on 11/6/2025 11:21:10 PM.
This article is licensed under a Creative Commons Attribution-NonCommercial 3.0 Unported Licence.

Check for updates

Cite this: *RSC Adv.*, 2018, **8**, 23019

Enhanced device performance and stability of perovskite solar cells with low-temperature ZnO/TiO_2 bilayered electron transport layers†

Caifeng Zhang,[abc] Guangmei Zhai,*[abc] Yong Zhang,[acd] Wenhui Gao,[ac] Zhimeng Shao,[ac] Lulu Zheng,[ac] Fuhong Mei,[ac] Hua Zhang,*[ac] Yongzhen Yang,[ac] Xuemin Li,[ac] Xuguang Liu[acd] and Bingshe Xu[ac]

The instability of perovskite films is a major issue for perovskite solar cells based on ZnO electron transport layers (ETLs). Here, ZnO nanoparticle (NP)- and ZnO sol–gel layers capped with low-temperature processed TiO_2, namely ZnO/TiO_2 bilayered films, have been successfully employed as ETLs in highly efficient $MAPbI_3$-based perovskite solar cells. It is demonstrated that these ZnO/TiO_2 bilayered ETLs are not only capable of enhancing photovoltaic performance, but also capable of improving device stability. The best device based on the ZnO/TiO_2 bilayered ETL exhibits an efficiency of ~15% under standard test conditions and can retain nearly 100% of its initial efficiency after 30 days of atmosphere storage, showing much higher device performance and stability compared to those devices based on ZnO single-layer ETLs. Moreover, it is found that perovskite films and devices prepared on the single ZnO sol–gel ETLs are much superior to those deposited on the single ZnO NP-ETLs in both stability and performance, which can be ascribed to fewer surface hydroxyl groups and much smoother surface morphology of the ZnO sol–gel films. The results pave the way for ZnO to be used as an effective ETL of low-temperature processed, efficient and stable PSCs compatible with flexible substrates.

Received 13th April 2018
Accepted 19th June 2018

DOI: 10.1039/c8ra03162b

rsc.li/rsc-advances

Introduction

Organic–inorganic hybrid perovskite solar cells (PSCs) have drawn much attention in the past several years as the power conversion efficiency (PCE) increases quickly from preliminary 3.8% to 22.7% in the present day.[1,2] Although the excellent performance of PSCs is fundamentally due to perovskite materials' excellent electronic and optical properties, such as direct bandgap structures, high light absorption coefficients, high carrier mobilities, low exciton binding energies and long carrier diffusion lengths,[3–5] technically it is also related to their device structure. PSCs either in a normal (n–i–p) structure or an inverted (p–i–n) structure are generally composed of a transparent conductive layer, an electron transport layer (ETL), a light absorption perovskite layer, a hole transport layer and a metal electrode layer. Among these layers, ETL works as an electron selective contact, playing an important role in extracting electrons from the light absorbing layer and suppressing charge recombination,[6–8] and thus significantly affects the final performance of PSCs. To date, the most widely used ETL material in perovskite photovoltaic devices is TiO_2, based on which highly efficient PSCs with power conversion efficiencies exceeding 20% have been produced. However, TiO_2 usually requires a high sintering temperature (~500 °C) to obtain its anatase phase for most of the highly efficient perovskite devices in the normal device structure, which not only increases their producing cost but also hinders the development of flexible devices on plastic substrates.[9] Therefore, the exploration of low-temperature processed ETLs for PSCs is highly desirable. So far, several low-temperature processable ETL materials including ZnO[8] and SnO_2[10,11] have been developed. Specifically, as a wide band gap semiconductor, ZnO can achieve high crystalline quality even at low temperature.[12] Moreover, ZnO has a suitable work function, outstanding light transmittance and a high electron mobility.[13] All of these remarkable optoelectronic properties of ZnO make it an attractive ETL candidate in PSCs. Some efforts have been made in low-temperature ZnO-based PSCs. Kelly *et al.*[8] successfully employed ZnO nanoparticle (NP)-ETLs to fabricate $CH_3NH_3PbI_3$-based planar heterojunction PSCs with high efficiency at room temperature. Elumalai and Uddin *et al.*[14] used a simple, low-temperature (<150

[a]*Key Laboratory of Interface Science and Engineering in Advanced Materials of Ministry of Education, Research Centre of Advanced Materials Science and Technology, Taiyuan University of Technology, Taiyuan, Shanxi 030024, China. E-mail: zhaiguangmei@tyut.edu.cn; zhanghua01@tyut.edu.cn*

[b]*CAS Key Laboratory of Renewable Energy, Guangzhou 510640, China*

[c]*Collaborative Innovation Centre for Advanced Thin-film Optoelectronic Materials and Devices in Shanxi Province, Taiyuan, Shanxi 030024, China*

[d]*College of Materials Science and Engineering, Taiyuan University of Technology, Taiyuan, Shanxi 030024, China*

† Electronic supplementary information (ESI) available: [Fig. S1–Fig. S9]. See DOI: 10.1039/c8ra03162b

Open Access Article. Published on 22 June 2018. Downloaded on 11/6/2025 11:21:10 PM.
This article is licensed under a Creative Commons Attribution-NonCommercial 3.0 Unported Licence.

°C) processed sol–gel ZnO thin film as ETL for $CH_3NH_3PbI_3$-based perovskite solar cells and achieved a PCE of 8.77%. However, perovskite films deposited atop ZnO layers encounter a severe instability issue, which would adversely affect the application of these devices.[15,16] To alleviate the instability problem, several strategies have been reported, such as doping[17,18] and surface modification/passivation.[15,19] Although the stability of ZnO based devices has been indeed improved by means of these strategies, either their performance is still poor or high-temperature processes are involved in some strategies.

In this work, we develop a facile and effective method of improving the stability of ZnO-based PSCs, in which low-temperature processed TiO_2 was deposited on top of either ZnO NP- or ZnO sol–gel layers to form ZnO/TiO_2 bilayered ETLs for perovskite solar cells. Compared with those ZnO single-layer ETLs, not only stability but also photovoltaic performance of the devices based on the ZnO/TiO_2 bilayer-ETLs was substantially enhanced. Moreover, interestingly we found that the perovskite films prepared *via* "one-step" deposition on the ZnO sol–gel ETLs are much superior to those deposited on the ZnO NP-ETLs in both stability and device performance. Since the entire device fabrication can be processed at less than 150 °C, it is expected that the ZnO/TiO_2 bilayer-ETLs reported here would have great application potential in flexible devices with roll-to-roll processes.

Experimental

Materials

Ti-nanoxide T-L/SC was purchased from Solaronix, Switzerland. *N*,*N*-dimethylformamide (DMF, ≥99.8%), dimethyl sulfoxide (DMSO, ≥99.5%), chlorobenzene (99.8%), acetonitrile (99.9%), 4-*tert*-butylpyridine (TBP, >96.0%), and bistrifluoromethanesulfonimide lithium (Li-TFSI, 99.95%) were ordered from Sigma-Aldrich. Lead iodide (PbI_2, 99.999%) and CH_3NH_3I (MAI, 99%) were obtained from Shanghai MaterWin New Materials Co., Ltd. Diethyl ether, zinc acetate dihydrate, methanol, *n*-butanol, chloroform, 2-methoxyethanol, ethanolamine were purchased from Sinopharm Chemical Reagent Co., Ltd. 2,2′,7,7′-tetrakis[*N*,*N*-Di(4-methoxyphenyl)amino]-9,9′-spiro-bifluorene (spiro-OMeTAD, >99.5%) and gold electrode (99.999%) were ordered from Luminescence Technology Corp. and Zhongnuo Advanced Material Technology Co., Ltd, respectively. All the chemicals were used as received without any further purification.

Device fabrication

The ZnO NPs and ZnO sol–gel were prepared according to the methods reported in literatures 8 and 20, respectively. All of the devices were fabricated on fluorine-doped tin oxide (FTO, 7 ± 1 Ω □$^{-1}$) glass substrates. These FTO substrates were cleaned orderly by ultrasonication in detergent, DI water, acetone and ethanol for 15 min, respectively. Then the substrates were blow dried with N_2 and treated with ultraviolet/ozone for 15 min before the fabrication of solar cells. For the ZnO-NP films, the as-prepared ZnO NP-solution (around 6 mg mL^{-1} in the mixture of *n*-butanol, methanol and chloroform) was spin-coated onto the substrate at 2500 rpm for 30 s and then annealed on a hot plate at 130 °C for 10 min in air. The procedure was repeated again to obtain a continuous, smooth film. For the ZnO sol–gel films deposited by a low temperature method, the ZnO sol–gel precursor solution was spin-coated onto the substrate at 4000 rpm for 30 s and then annealed on a hot plate at 140 °C for 30 min in air. The procedure was also repeated once. To construct the ZnO NPs/TiO_2 and ZnO sol–gel/TiO_2 bilayered films, the Ti-nanoxide T-L/SC was first diluted to half of its original concentration in order to get an optimal film thickness. Then the solution was spin-coated onto the ZnO-NP film or ZnO sol–gel film at 4000 rpm for 30 s, followed by annealing at 150 °C for 30 min. The thicknesses of these ZnO-NP, ZnO sol–gel, and TiO_2-NP films are around 50 nm, 50 nm, and 60 nm, respectively. Then the substrates were transferred into a N_2-filled glovebox. The perovskite layers were deposited on the obtained ETLs by a "one-step" deposition method.[21] The perovskite precursor solution containing 484 mg PbI_2, 159 mg MAI and 71 μL DMSO (molar ratio 1.05 : 1 : 1) in 635 μL DMF was spin-coated at 4000 rpm for 30 s, and then 500 μL of diethyl ether was continuously dripped onto the rotating substrate in 8 s. Subsequently the as-prepared transparent intermediate phase films were heated in order at 65 °C for 1 min and at 100 °C for 2 min to obtain compact perovskite films. After cooling down to room temperature, a spiro-OMeTAD based HTL precursor [72.3 mg spiro-OMeTAD, 29 μL TBP and 18 μL Li-TFSI solution (520 mg mL^{-1} Li-TFSI solution in acetonitrile) all dissolved in 1 mL chlorobenzene] was spin-coated on the perovskite layer at 3000 rpm for 30 s to form a smooth HTL. Then the samples with HTL were left overnight in an electronic dry cabinet (≤15% RH) for oxidation. Finally, an Au electrode was deposited on top of the spiro-OMeTAD layer by thermal evaporation.

Characterization

The X-ray diffraction (XRD) with Cu Kα radiation (1.5418 Å) was performed on a Y-2000 Automated X-ray diffractometer or a Rigaku Smart Lab SE X-ray diffractometer. The Fourier transform infrared (FT-IR) spectra were recorded on a Bruker Tensor 27 infrared spectrometer. The surface chemical compositions of films were characterized by X-ray photoelectron spectroscopy (XPS, ESCALAB 250Xi, Thermo Fisher). The surface morphologies of films were obtained using a JSM-6700F field emission scanning electron microscope (SEM) and the surface roughness was measured with a NSK SPA-300HV atomic force microscope (AFM). The absorbance and transmittance spectra were recorded by a Perkin Elmer Lambda 950 UV-Vis-NIR spectrometer. The current density–voltage (*J*–*V*) characteristics of the devices were measured with a PVIV-3A solar cell measurement system including a solar simulator and a Keithley 2400 source meter at room temperature. The AM 1.5G illumination of 100 mW cm^{-2} was calibrated by using a standard Si reference cell certificated by the National Institute of Metrology, China. The effective area of cells was defined as 3 mm^2.

Open Access Article. Published on 22 June 2018. Downloaded on 11/6/2025 11:21:10 PM.
This article is licensed under a Creative Commons Attribution-NonCommercial 3.0 Unported Licence.

Results and discussion

Fig. 1 shows the transmittance spectra and SEM images of a ZnO-NP film, a ZnO sol–gel film, a ZnO NPs/TiO_2 bilayered film and a ZnO sol–gel/TiO_2 bilayered film. It can be clearly seen from Fig. 1(a) and (d) that both the ZnO-NP film and the ZnO sol–gel film possess similar transmittance values (≥80%) to those of their ZnO/TiO_2 bilayered counterparts over the entire spectral range from 400 nm to 800 nm, indicating that the TiO_2 capping layers have no negative effects on ETLs' optical characteristics. The SEM images [Fig. 1(b), (c), (e) and (f)] show that the ZnO-NP film is much rougher than the ZnO sol–gel film, causing the slightly uneven surface of the ZnO NPs/TiO_2 bilayered film compared to the ZnO sol–gel/TiO_2 bilayered film, while both TiO_2 top layers are relatively dense. The XRD patterns of these films were obtained by grazing-incidence X-ray diffraction measurements and shown in Fig. S1.† As can be seen from Fig. S1,† (100), (101) and (110) characteristic diffraction peaks of hexagonal ZnO at $2\theta = 31.6°$, 36.1° and 56.6°, respectively, are distinguishable for the ZnO-NP film. However, no clear characteristic peaks can be observed for the ZnO sol–gel film, indicating that the crystallization of the ZnO sol–gel film is much worse than the ZnO-NP film. Moreover, only weak (101) characteristic diffraction peaks of anatase TiO_2 at $2\theta = 25.3°$ can be observed in the XRD patterns of those ZnO NPs/TiO_2, ZnO sol–gel/TiO_2, and TiO_2 films, suggesting that these low-temperature ETLs are less crystallized.

Following the processes stated in the experimental section, $MAPbI_3$ perovskite films were deposited on these four ETLs and then annealed in N_2 at 100 °C to evaluate their stability. Fig. 2(a) shows the photographs of $MAPbI_3$ films deposited on the ZnO-NP film and the ZnO NPs/TiO_2 bilayered film before and after the thermal treatment. It can be seen that both $MAPbI_3$ films on the ZnO-NP film and the ZnO NPs/TiO_2 bilayered film are initially dark brown. After annealing at 100 °C for 10 min, the $MAPbI_3$ film on the ZnO-NP film turned light brown, indicating that the perovskite film had partly decomposed. When the annealing time was prolonged to 20 min, the $MAPbI_3$ film on the ZnO-NP film had predominantly become yellowish, reflecting a basically complete decomposition of perovskite into PbI_2. However, the $MAPbI_3$ perovskite film on the ZnO NPs/TiO_2 bilayered film was still dark brown after annealing for 20 min and could even remain unchanged in a prolonged period of time, manifesting that the low-temperature ZnO NPs/TiO_2 bilayered film can significantly improve the stability of perovskite films compared with the single ZnO-NP film. Fig. 2(b) shows the photographs of $MAPbI_3$ films on the ZnO sol–gel film and the ZnO sol–gel/TiO_2 bilayered film before and after the thermal treatment. At the beginning, the $MAPbI_3$ films deposited on both the ZnO sol–gel film and the ZnO sol–gel/TiO_2 film are also dark brown, same as those on the ZnO-NP film and the ZnO NPs/TiO_2 film. Unexpectedly, the $MAPbI_3$ film deposited on the ZnO sol–gel film showed much higher thermal stability than that on the ZnO-NP film. As shown in Fig. 2(b), even after annealing at 100 °C for 100 min, only the marginal part of the film slightly turned yellow while the most area still remained the same dark brown as the perovskite on the ZnO sol–gel-TiO_2 bilayered film. This indicates that the stability of perovskite on the ZnO sol–gel films is only slightly lower than that on the ZnO sol–gel/TiO_2 bilayered films, but much higher than that on the ZnO-NP films.

In order to understand their difference in stability, we investigated the surface chemistry of these four ETLs by XPS measurements. As shown in Fig. 3, the O 1s core level spectra can be deconvoluted into two main peaks located at 530.0 eV (or 529.5 eV) and 531.4 eV, which correspond to the O 1s core level

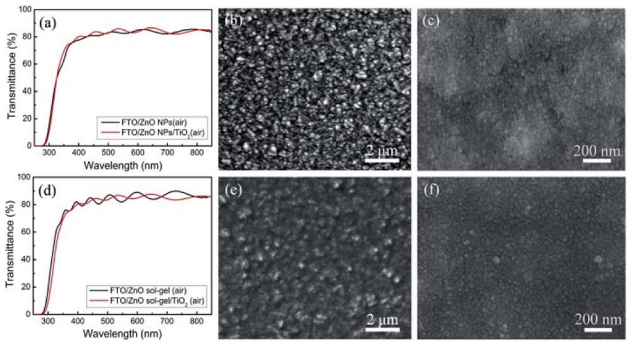

Fig. 1 Transmittance spectra (a and d) and SEM images of (b) a ZnO-NP film, (c) a ZnO NPs/TiO_2 bilayered film, (e) a ZnO sol–gel film, and (f) a ZnO sol–gel/TiO_2 bilayered film.

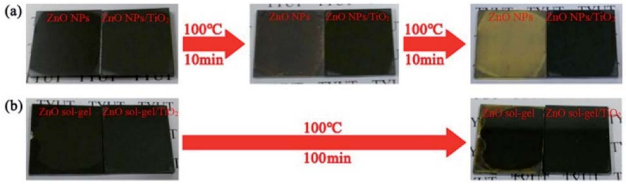

Fig. 2 The stability comparison between perovskite films deposited (a) on a ZnO-NP film and a ZnO NPs/TiO_2 bilayered film, (b) on a ZnO sol–gel film and a ZnO sol–gel/TiO_2 bilayered film upon thermal treatments.

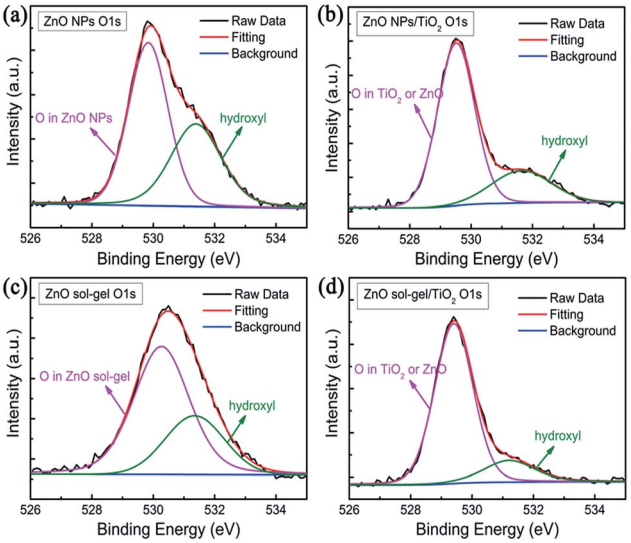

Fig. 3 XPS spectra of (a) a ZnO-NP film, (b) a ZnO NPs/TiO_2 bilayered film, (c) a ZnO sol–gel film, and (d) a ZnO sol–gel/TiO_2 bilayered film.

Open Access Article. Published on 22 June 2018. Downloaded on 11/6/2025 11:21:10 PM.
This article is licensed under a Creative Commons Attribution-NonCommercial 3.0 Unported Licence.

in ZnO (and/or TiO_2) and the chemisorbed oxygen species such as hydroxyl (OH^-), respectively. Their Zn 2p and Ti 2p core level spectra are shown in Fig. S2.† It is generally believed that hydroxyls on the surface of ZnO are the origin of the decomposition of perovskite.[15,16] Hydroxyls on the film surface are derived from dissociated and molecularly adsorbed water.[22] For the ZnO-NP film, the ratio of O in hydroxyls and O in ZnO NPs is 0.688 : 1, however the ratio of O in hydroxyls and O in TiO_2 (and/or ZnO NPs) decreases to 0.307 : 1 for the ZnO NPs/TiO_2 bilayered film, which we believe can account for the improved thermal stability of perovskite films on the ZnO NPs/TiO_2 bilayered films in comparison with the ZnO-NP films. Similarly, the ratios are 0.436 : 1 and 0.194 : 1 for the ZnO sol–gel film and the ZnO sol–gel/TiO_2 bilayered film, respectively, which may be responsible for the improved thermal stability of perovskite films on the bilayered ETLs to some extent. Moreover, it is obvious that the ratio of hydroxyls in the ZnO sol–gel is significantly lower than that in the ZnO NPs, and even comparable to that in ZnO NPs/TiO_2 bilayered films. Therefore, we believe that the better thermal stability for perovskite films on the ZnO sol–gel films as compared to the ZnO-NP films can be, at least partly, ascribed to fewer hydroxyls on the surface of the ZnO sol–gel films. Fewer hydroxyls on the ZnO sol–gel film surface probably result from its relatively smooth surface where less molecularly water can be absorbed.[22] Also, we employed FT-IR to investigate chemical groups in the ZnO-NP films and the ZnO sol–gel films. As shown in Fig. S3,† the peak associated to the stretching of hydroxyls around 3400 cm^{-1} in the ZnO sol–gel sample is obviously stronger than that in the ZnO NP-sample, which seems to be contradictory to the XPS results presented above. However, given that the ZnO sol–gel film is formed by polycondensation reaction and less crystalized (which can be supported by XRD results discussed above), much more hydroxyl groups should exist inside the ZnO sol–gel film than the ZnO-NP film. Moreover, FT-IR is a technique commonly used to probe bulk properties of materials rather than their surface properties which XPS is capable of characterizing. We believe that the inconsistency is understandable and the decomposition of perovskite is predominately caused by hydroxyl groups on the ZnO film surface rather than inside the film. In addition, to gain more insights into possible reasons for the stability difference between perovskite films on these two kinds of ZnO, their surface topography was further characterized *via* AFM measurements (Fig. 4). Consistent with the top-view SEM results, the root mean square (RMS) roughness of the ZnO-NP film (32.63 nm) is much higher than that of the ZnO sol–gel film (5.695 nm). The rougher surfaces of ZnO-NP films provide more contact area with perovskite, leading to the deteriorated thermal stability of perovksite.

Fig. 5 shows the SEM images of perovskite films on these four different ETLs. It can be seen that the morphology of the perovskite film deposited on the ZnO-NP film is clearly different from that on the ZnO sol–gel film. The former is composed of bigger grains with size of around 200 nm and a few voids, which is probably induced by the release of gas byproducts from perovskite decomposition,[23] whereas the latter is flat and dense, and made of smaller grains of about 100 nm. It is speculated

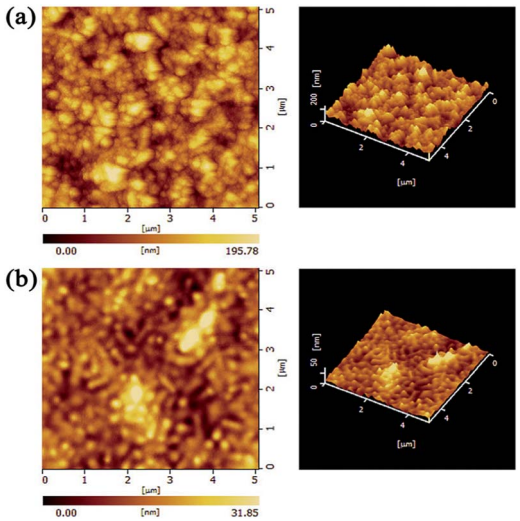

Fig. 4 Two and three dimensional AFM images of (a) a ZnO-NP film, (b) a ZnO sol–gel film.

that the different morphologies between these two samples is due to the occurrence of distinct nucleation and crystal growth processes caused by different underlying ETLs.[24,25] The perovskite films on the ZnO NPs/TiO_2 film and the ZnO sol–gel/TiO_2 film have very similar surface morphology owing to the existence of the same underlying TiO_2 layers.

Using the perovskite films deposited on these four ETLs, we further fabricated PSCs with the structure of FTO/ETL/$CH_3NH_3PbI_3$/spiro-OMeTAD/Au, as illustrated in Fig. 6(a), in order to investigate the effects of underlying ETLs on device performance and stability (the cross-sectional SEM image of a typical actual device is shown in Fig. S4†). These devices' schematic energy band diagram is shown in Fig. 6(b). The optimized thicknesses of the ZnO-NP films, ZnO sol–gel films, TiO_2 capping layers, perovskite films, spiro-OMeTAD films and Au films are 50 nm, 50 nm, 60 nm, 450 nm, 190 nm and 60 nm,

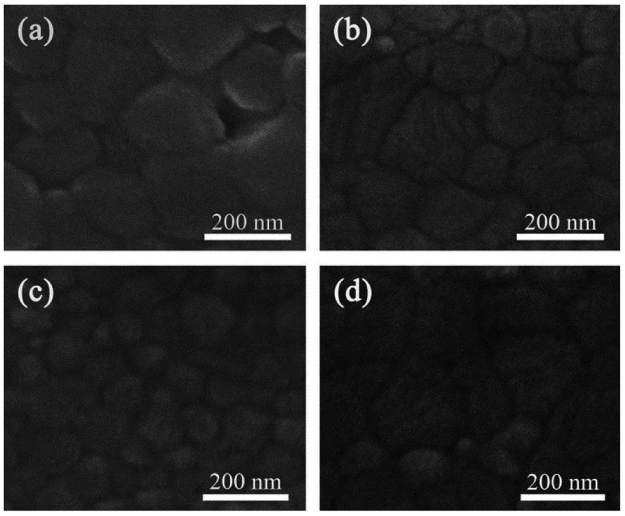

Fig. 5 SEM images of perovskite films deposited on (a) a ZnO-NP film, (b) a ZnO NPs/TiO_2 bilayered film, (c) a ZnO sol–gel film, and (d) a ZnO sol–gel/TiO_2 bilayered film, respectively.

Open Access Article. Published on 22 June 2018. Downloaded on 11/6/2025 11:21:10 PM.
This article is licensed under a Creative Commons Attribution-NonCommercial 3.0 Unported Licence.

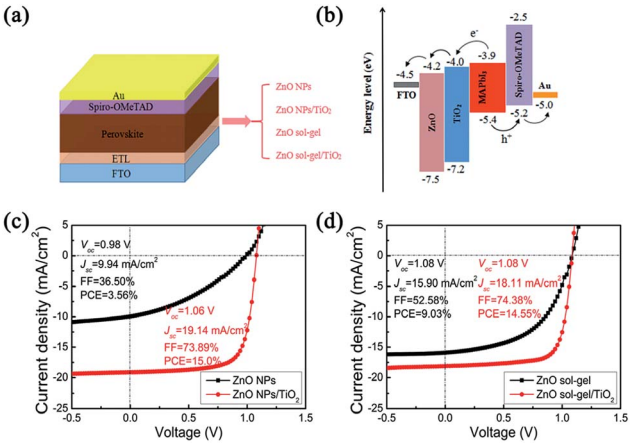

Fig. 6 (a) Schematic architecture of PSCs fabricated in the work; (b) schematic energy band diagram of PSCs fabricated in the work; typical J–V characteristics of perovskite solar cells fabricated (c) on a ZnO-NP film and a ZnO NPs/TiO_2 bilayered film; (d) on a ZnO sol–gel film and a ZnO sol–gel/TiO_2 bilayered film.

respectively. Statistics results of photovoltaic parameters, series resistance (R_s) and shunt resistance (R_{sh}) for PSCs fabricated on the ZnO-NP films, ZnO NPs/TiO_2 bilayered films, ZnO sol–gel films and ZnO sol–gel/TiO_2 bilayered films are tabulated in Table 1. The typical current density–voltage (J–V) characteristics of the PSCs based on these four ETLs under AM 1.5G 100 mW cm^{-2} simulated solar light are shown in Fig. 6(c) and (d). The device with the ZnO NP-ETL, as shown in Fig. 6(c), exhibits a poor PCE of 3.56% with an open circuit voltage (V_{oc}) of 0.98 V, a short-circuit current density (J_{sc}) of 9.94 mA cm^{-2}, and a fill factor (FF) of 36.50%, while the device containing the ZnO NPs/TiO_2 bilayered ETL yields a dramatically enhanced PCE of 15.0% with a V_{oc} of 1.06 V, a J_{sc} of 19.1 mA cm^{-2}, and a FF of 73.9%. Also, it can be clearly seen from Fig. 6(d) that the device based on the ZnO sol–gel/TiO_2 bilayered ETL shows a high PCE of 14.55% with a V_{oc} of 1.08 V, a J_{sc} of 18.11 mA cm^{-2}, and a FF of 74.38%. In contrast, a decent PCE of 9.03% can only be achieved for the device with the ZnO sol–gel single-layer ETL due to the reduced J_{sc} (15.90 mA cm^{-2}) and FF (52.58%). We note that, as shown in Fig. S5 and Table S1,† the hysteresis of these devices based on low-temperature ETLs is serious probably due to the existence of a large number of defects in these ETL materials.[26] But then, devices based on the ZnO/TiO_2 bilayered ETLs show less hysteresis than the corresponding ZnO-only devices.

To elucidate the influence of these underlying ETLs on perovskite properties and device performance, a variety of structural, optical and electrical measurements on the perovskite films and devices were further conducted. For the perovskite films deposited on the ZnO NP-ETL and the ZnO NPs/TiO_2 bilayered ETL, XRD patterns [Fig. 7(a)] show that, as expected, there is a characteristic diffraction peak of PbI_2 (001) at around 12.8° for the perovskite film on the ZnO NP-ETL, suggesting a fast decomposition of $MAPbI_3$ into PbI_2 in the course of device fabrication. However, the peak is missing for the perovskite film on the ZnO NPs/TiO_2 bilayered ETL, which indicates that the decomposition of perovskite on the ZnO NPs/TiO_2 bilayered film has been effectively suppressed. This is consistent with the results of the accelerated degradation experiment shown in Fig. 2. The absorbance spectra of both perovskite films are shown in Fig. 8(a). It can be seen that the absorption intensity of the perovskite film on the ZnO NP-ETL is slightly lower than that on the ZnO/TiO_2 bilayered ETL, and an shoulder around 498 nm only occurs in the former's absorption spectrum, further indicating the decomposition of perovskite on the ZnO NP-ETL into PbI_2.[27] The degradation of perovskite does not have too much influence on V_{oc}, but reduces J_{sc} and FF remarkably, thereby adversely affecting the final device performance. It could be ascribed to the increased series resistance and associated recombination as a consequence of inhomogeneous degradation of the perovskite film.[28] As tabulated in Table 1, the devices containing these ZnO NPs/TiO_2 bilayered ETLs have much lower series resistance (R_s) and remarkably higher shunt resistance (R_{sh}) calculated from J–V curves than the cells based on those ZnO NP-ETLs.

For the perovskite films deposited on the ZnO sol–gel ETL and the ZnO sol–gel/TiO_2 bilayered ETL, as shown in Fig. 7(b), no characteristic diffraction peaks of PbI_2 can be detected. Moreover, the absorption intensity of perovskite on the ZnO sol–gel ETL is almost the same as that on the ZnO sol–gel/TiO_2 bilayered ETL [Fig. 8(b)]. Therefore, the enhanced performance for devices on the ZnO sol–gel/TiO_2 bilayered films may be not mainly due to the suppressed decomposition of perovskite, though they have lower R_s and higher R_{sh} compared to those on the ZnO sol–gel ETLs, as tabulated in Table 1. To further investigate possible reasons for the improved efficiency, time-resolved photoluminescence (TRPL) measurements of perovskite films deposited on the ZnO sol–gel film and the ZnO sol–gel/TiO_2 bilayered film were performed and displayed in Fig. 9. The TRPL spectra of the perovskite films on both ETLs show bi-exponential decays with fast (τ_1) and slow (τ_2) components, and the resulting decay lifetimes and decay amplitudes (A_i) are listed

Table 1 Statistics of photovoltaic parameters, series resistance (R_s) and shunt resistance (R_{sh}) of perovskite solar cells fabricated on ZnO-NP films, ZnO NPs/TiO_2 bilayered films, ZnO sol–gel films and ZnO sol–gel/TiO_2 bilayered films

ETL	V_{oc} (V)	J_{sc} (mA cm^{-2})	FF (%)	PCE (%)	R_s/Ohm	R_{sh}/Ohm
ZnO NPs	0.94 ± 0.03	9.40 ± 0.68	35.46 ± 2.86	3.12 ± 0.15	2086 ± 172	10 948 ± 1333
ZnO NPs/TiO_2	1.06 ± 0.007	18.89 ± 0.37	71.95 ± 2.63	14.44 ± 0.43	263 ± 15	53 427 ± 5253
ZnO sol–gel	1.06 ± 0.01	15.53 ± 0.22	51.50 ± 0.98	8.48 ± 0.27	679 ± 41	18 807 ± 1452
ZnO sol–gel/TiO_2	1.06 ± 0.008	18.04 ± 0.13	74.31 ± 0.32	14.26 ± 0.16	250 ± 15	49 756 ± 4490

Open Access Article. Published on 22 June 2018. Downloaded on 11/6/2025 11:21:10 PM.
This article is licensed under a Creative Commons Attribution-NonCommercial 3.0 Unported Licence.

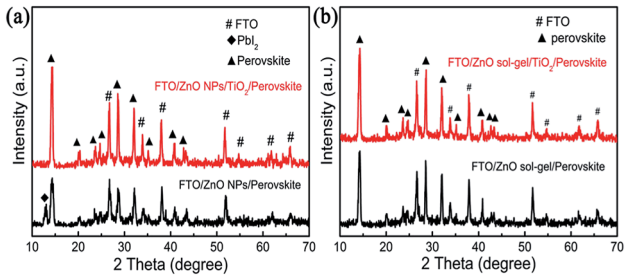

Fig. 7 XRD patterns of perovskite films deposited (a) on a ZnO-NP film and a ZnO NPs/TiO_2 bilayered film; (b) on a ZnO sol–gel film and a ZnO sol–gel/TiO_2 bilayered film.

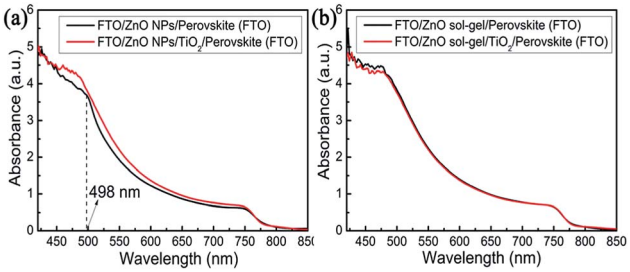

Fig. 8 Absorbance spectra of perovskite films deposited (a) on a ZnO NP-film and a ZnO NPs/TiO_2 bilayered film; (b) on a ZnO sol–gel film and a ZnO sol–gel/TiO_2 bilayered film.

in the inset of Fig. 9. It is reported that τ_1 is a decay component closely related to non-radiative recombination by defects (*e.g.* surface traps near grain boundaries), while τ_2 is a component of radiative recombination from bulk perovskite.[17,29] As shown in Fig. 9 and its inset, on one hand, the perovskite on the ZnO sol–gel/TiO_2 bilayered film has a much longer lifetime τ_1 compared to the perovskite deposited on the ZnO sol–gel film, suggesting it has fewer traps near grain boundaries. This is in consistence with the results deduced from the SEM images (Fig. 5) that the perovskite on the ZnO sol–gel film has more grain boundaries due to their smaller grain size. On the other hand, perovskite on the ZnO sol–gel/TiO_2 bilayered film has a much shorter lifetime τ_2 compared to perovskite deposited on the ZnO sol–gel film,

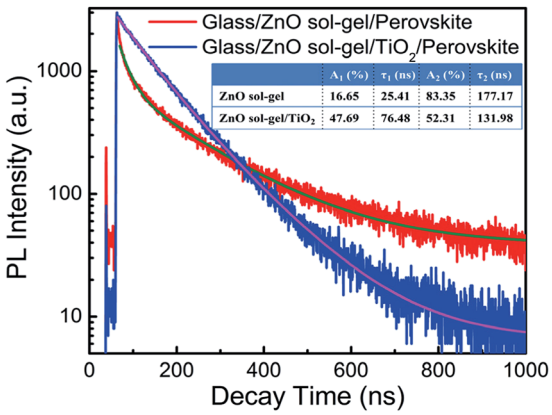

	A_1 (%)	τ_1 (ns)	A_2 (%)	τ_2 (ns)
ZnO sol-gel	16.65	25.41	83.35	177.17
ZnO sol-gel/TiO_2	47.69	76.48	52.31	131.98

Fig. 9 Time resolved photoluminescence spectra of perovskite films deposited on a ZnO sol–gel film and a ZnO sol–gel/TiO_2 bilayered film. Inset: the resulting decay lifetimes (τ_i) and decay amplitudes (A_i).

implying that the electron transfer from perovskite to the ZnO sol–gel/TiO_2 bilayered film is faster than the ZnO sol–gel film. According to the equation $\tau_{ave} = \sum A_i\tau_i^2/\sum A_i\tau_i$, the estimated average carrier lifetimes (τ_{ave}) in these perovskite films deposited on the ZnO sol–gel and ZnO sol–gel/TiO_2 films are 172.94 ns and 112.79 ns, respectively. The more efficient carrier extraction between perovskite and the ZnO sol–gel/TiO_2 bilayer-ETL is further confirmed by the weaker steady-state PL in comparison with perovskite on the ZnO sol–gel film, as shown in Fig. S6.† The more efficient carrier extraction in the ZnO sol–gel/TiO_2 bilayer-based device results in a higher J_{sc}.[30,31] The higher FF for the ZnO sol–gel/TiO_2 bilayer-ETL device can be ascribed to its lower R_s and higher R_{sh}, as shown in Table 1.[31,32] In addition, although the conductivity of the ZnO sol–gel film is much lower than that of the ZnO-NP film (Fig. S7†), it is evident that the device performance based on the ZnO sol–gel ETL is far superior to the device based on the ZnO NP-ETL, which can be attributed to the fact that perovskite on the ZnO sol–gel films is much more stable. As shown in Fig. S8,† the more stable perovskite film on the ZnO sol–gel film behaves better in light harvesting compared to that on the ZnO-NP film. As mentioned above, the appearance of a shoulder at around 498 nm for the perovskite/ZnO-NP film indicates the partial decomposition of perovskite into PbI_2.[27]

Also, we fabricated perovskite solar cells based on low-temperature TiO_2-only ETLs to see if the performance enhancement just comes from the usage of TiO_2. The typical *J–V* curve of the TiO_2-only device is shown in Fig. S9.† When comparing the TiO_2-only device with those ZnO/TiO_2 devices, we can find that the former has a lower PCE than its bi-ETL counterparts mainly due to the reduced V_{oc} and FF. Therefore, we believe that the enhanced device performance after the introduction of TiO_2 is not only due to the fact that it may prevent the quick decomposition of perovskite, but also due to its synergistic effect with ZnO. For these ZnO/TiO_2 bilayered ETLs, the conduction band of TiO_2 is slightly higher than that of ZnO, which not only facilitates the electron injection from perovskite into ETL but also prevents the back electron transfer from ETL to perovksite.[19] Or, from another perspective, a n^+–n heterojunction might be formed at the ZnO/TiO_2 interface, where the induced built-in electrical field is beneficial to the suppression of interfacial charge recombination.[33] The reduced charge recombination at the perovskite/bilayered ETL interface is beneficial to increasing FF and V_{oc}.[19,34]

To evaluate device stability, unencapsulated devices fabricated on these four ETLs were stored in ambient environment (temperature: ~20 °C; relative humidity: ~20%) and tested under standard one sun illumination every few days. The plots of the normalized average PCEs as a function of storage time are shown in Fig. 10(a) and (b). The devices with the ZnO NP-ETLs drastically degraded and lost 75% of their initial efficiency merely within two days, showing considerably poor device stability. In contrast, the average efficiency of devices with the ZnO NPs/TiO_2 bilayer-ETLs increased first and then decreased, but nearly 100% of their initial efficiency was still retained even after thirty days, exhibiting much higher device stability. The initial device performance evolution was simultaneously

Open Access Article. Published on 22 June 2018. Downloaded on 11/6/2025 11:21:10 PM.
This article is licensed under a Creative Commons Attribution-NonCommercial 3.0 Unported Licence.

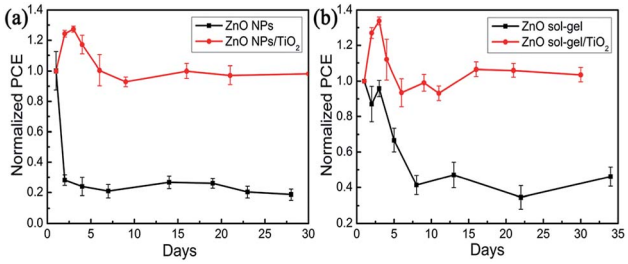

Fig. 10 Durability of perovskite solar cells fabricated (a) on a ZnO NP-film and a ZnO NPs/TiO_2 bilayered film; (b) on a ZnO sol–gel film and a ZnO sol–gel/TiO_2 bilayered film in air atmosphere (RH∼20%).

affected by two factors: spiro-OMeTAD oxidation and perovskite decomposition. The former can increase device efficiency, while the latter will degrade device performance. We note that the initial efficiency enhancement of these devices based on the bilayered ETLs might be attributed to the dominant spiro-OMeTAD oxidation, while the monotonic efficiency decline with the storage time for those devices based on the ZnO NP-ETLs results from their serious and predominant perovskite decomposition. Likewise, the average efficiency of devices with the ZnO sol–gel ETLs was only 40% of their initial value after eight days. However, the average efficiency of devices with the ZnO sol–gel/TiO_2 bilayered ETLs could remain their initial efficiency even after thirty days. Therefore, the ZnO/TiO_2 bilayer-ETLs reported in the work can not only significantly enhance device performance, but also effectively improve the device stability of ZnO-based PSCs.

Conclusions

The ZnO/TiO_2 bilayered films prepared by solution processes at low-temperature have been successfully employed as electron transport layers in $MAPbI_3$-based perovskite solar cells. The devices based on these low-temperature ZnO/TiO_2 bilayered ETLs exhibit not only high photovoltaic performance but also extraordinarily good stability compared with those based on ZnO single-layer ETLs. Moreover, it has been found that the perovskite films prepared on the ZnO sol–gel films are much superior to those deposited on the ZnO-NP films in both film stability and device performance, which can be ascribed to less surface hydroxyl groups and much smoother surface morphology in the ZnO sol–gel films. Our results suggest that the ZnO/TiO_2 bilayered films and even ZnO sol–gel films can be good ETL candidates for low-temperature PSCs, and pave the way for the fabrication of efficient and stable PSCs on flexible substrates.

Conflicts of interest

There are no conflicts of interest to declare.

Acknowledgements

This work was supported by the Basic Research Project of Shanxi Province (No. 201701D221079), the National Natural Science Foundation of China (No. 61475110), CAS Key Laboratory of Renewable Energy (No. Y807k31001) and the Youth Foundation of Taiyuan University of Technology (2015QN102). It was also partially supported by the National Natural Science Foundation of China (21471111, 61404089, 61504090, and 61604104), the National Key Research and Development Program of China (2016YFB0401803), the Basic Research Projects of Shanxi Province (2015021103 and 201601D202029), the Shanxi Provincial Key Innovative Research Team in Science and Technology (201605D131045-10), and the Platform and Base Special Project of Shanxi (201605D131038).

Notes and references

1 A. Kojima, K. Teshima, Y. Shirai and T. Miyasaka, *J. Am. Chem. Soc.*, 2009, **131**, 6050–6051.
2 http://www.nrel.gov/pv/assets/images/efficiency_chart.jpg (Rev. 12-15-2017).
3 C. C. Stoumpos, C. D. Malliakas and M. G. Kanatzidis, *Inorg. Chem.*, 2013, **52**, 9019–9038.
4 D. H. Fabini, J. G. Labram, A. J. Lehner, J. S. Bechtel, H. A. Evans, d. V. A. Van, F. Wudl, M. L. Chabinyc and R. Seshadri, *Inorg. Chem.*, 2017, **56**, 11–25.
5 S. D. Stranks, G. E. Eperon, G. Grancini, C. Menelaou, M. J. P. Alcocer, T. Leijtens, L. M. Herz, A. Petrozza and H. J. Snaith, *Science*, 2013, **342**, 341–344.
6 E. J. Juarez-Perez, M. Wuβler, F. Fabregat-Santiago, K. Lakus-Wollny, E. Mankel, T. Mayer, W. Jaegermann and I. Mora-Sero, *J. Phys. Chem. Lett.*, 2014, **5**, 680–685.
7 Q. Hu, J. Wu, C. Jiang, T. Liu, X. Que, R. Zhu and Q. Gong, *ACS Nano*, 2014, **8**, 10161–10167.
8 D. Liu and T. L. Kelly, *Nat. Photonics*, 2014, **8**, 133–138.
9 J. T. Wang, J. M. Ball, E. M. Barea, A. Abate, J. A. Alexander-webber, J. Huang, M. Saliba, I. Mora-sero, J. Bisquert, H. J. Snaith and R. J. Nicholas, *Nano Lett.*, 2013, **14**, 724–730.
10 Q. Jiang, L. Zhang, H. Wang, X. Yang, J. Meng, H. Liu, Z. Yin, J. Wu, X. Zhang and J. You, *Nat. Energy*, 2016, **2**, 16177.
11 Q. Liu, M. C. Qin, W. J. Ke, X. L. Zheng, Z. Chen, P. L. Qin, L. B. Xiong, H. W. Lei, J. W. Wan, J. Wen, G. Yang, J. J. Ma, Z. Y. Zhang and G. J. Fang, *Adv. Funct. Mater.*, 2016, **26**, 6069–6075.
12 T. Pauporté and I. Jirka, *Electrochim. Acta*, 2009, **54**, 7558–7564.
13 J. Song, W. Hu, X. F. Wang, G. Chen, W. Tian and T. Miyasaka, *J. Mater. Chem. A*, 2016, **4**, 8435–8443.
14 M. A. Mahmud, N. K. Elumalai, M. B. Upama, D. Wang, K. H. Chan, M. Wright, C. Xu, , F. Haque and A. Uddin, *Sol. Energy Mater. Sol. Cells*, 2017, **159**, 251–264.
15 Y. Cheng, Q. D. Yang, J. Xiao, Q. Xue, H. W. Li, Z. Guan, H. L. Yip and S. W. Tsang, *ACS Appl. Mater. Interfaces*, 2015, **7**, 19986–19993.
16 J. Yang, B. D. Siempelkamp, E. Mosconi, F. D. Angelis and T. L. Kelly, *Chem. Mater.*, 2015, **27**, 4229–4236.
17 Z. L. Tseng, C. H. Chiang, S. H. Chang and C. G. Wu, *Nano Energy*, 2016, **28**, 311–318.
18 J. Song, E. Zheng, L. Liu, X. F. Wang, G. Chen, W. Tian and T. Miyasaka, *ChemSusChem*, 2016, **9**, 1–9.

Open Access Article. Published on 22 June 2018. Downloaded on 11/6/2025 11:21:10 PM.
This article is licensed under a Creative Commons Attribution-NonCommercial 3.0 Unported Licence.

19 P. Chen, X. Yin, M. Que, Y. Yang and W. Que, *RSC Adv.*, 2016, **6**, 57996–58002.
20 Y. Sun, J. H. Seo, C. J. Takacs, J. Seifter and A. J. Heeger, *Adv. Mater.*, 2011, **23**, 1679–1683.
21 N. Ahn, D. Y. Son, I. H. Jang, S. M. Kang, M. Choi and N. G. Park, *J. Am. Chem. Soc.*, 2015, **137**, 8696–8699.
22 K. Yadav, B. R. Mehta, S. Bhattacharya and J. P. Singh, *Sci. Rep.*, 2016, **6**, 35073.
23 G. S. Han, H. W. Shim, S. Lee, M. L. Duff and J. K. Lee, *ChemSusChem*, 2017, **10**, 2425–2430.
24 J. Zhang and T. Pauporté, *J. Phys. Chem. C*, 2015, **119**, 14919–14928.
25 C. Bi, Q. Wang, Y. Shao, Y. Yuan, Z. Xiao and J. Huang, *Nat. Commun.*, 2015, **6**, 7747.
26 X. Cao, L. Zhi, Y. Li, X. Cui, L. Ci, K. Ding and J. Wei, *RSC Adv.*, 2017, **7**, 49144–49150.
27 J. Zhang, G. Zhai, W. Gao, C. Zhang, Z. Shao, F. Mei, J. Zhang, Y. Yang, X. Liu and B. Xu, *J. Mater. Chem. A*, 2017, **5**, 4190–4198.
28 B. Conings, J. Drijkoningen, N. Gauquelin, A. Babayigit, J. D'Haen, L. D'Olieslaeger, A. Ethirajan, J. Verbeeck, J. Manca and E. Mosconi, *Adv. Energy Mater.*, 2015, **5**, 1500477.
29 D. Y. Son, J. W. Lee, Y. J. Choi, I. H. Jang, S. Lee, P. J. Yoo, H. Shin, N. Ahn, M. Choi, D. Kim and N. G. Park, *Nat. Energy*, 2016, **1**, 16081.
30 Q. Dong, Y. Shi, K. Wang, Y. Li, S. Wang, H. Zhang, Y. Xing, Y. Du, X. Bai and T. Ma, *J. Phys. Chem. C*, 2015, **119**, 10212–10217.
31 B. X. Chen, H. S. Rao, W. G. Li, Y. F. Xu, H. Y. Chen, D. B. Kuang and C. Y. Su, *J. Mater. Chem. A*, 2016, **4**, 5647–5653.
32 J. Wang, M. Qin, H. Tao, W. Ke, Z. Chen, J. Wan, P. Qin, L. Xiong, H. Lei, H. Yu and G. Fang, *Appl. Phys. Lett.*, 2015, **106**, 121104.
33 M. Law, L. E. Greene, A. Radenovic, T. Kuykendall, J. Liphardt and P. Yang, *J. Phys. Chem. B*, 2006, **110**, 22652–22663.
34 J. Xu, Z. Chen, J. A. Zapien, C. S. Lee and W. Zhang, *Adv. Mater.*, 2014, **26**, 5337–5367.

 This journal is © The Royal Society of Chemistry 2018